RSC Advances

PAPER

View Article Online
View Journal | View Issue

Cite this: *RSC Adv.*, 2021, **11**, 31572

Synthesis and characterization of polyaniline–hydrotalcite–graphene oxide composite and application in polyurethane coating

Boi An Tran, *[ac] Huynh Thanh Linh Duong,[a] Thi Xuan Hang To[bc] and Thanh Thao Phan[ac]

In this paper, a composite from polyaniline and graphene oxide-hydrotalcite hybrid (PAN–HG) was fabricated by direct polymerization of aniline using ammonium persulphate as an oxidant in the presence of a HG hybrid. The structure and morphological properties of synthesized PAN–HG composites were characterized by Fourier transform infrared (FTIR) spectroscopy, X-ray diffraction (XRD), Raman spectra, and scanning electron microscopy (SEM) techniques. The electrochemical properties of the composite particles were also analyzed by potentiodynamic polarization curves to evaluate the corrosion inhabitation. The results were calculated by Tafel fitting and showed that the effective corrosion protection values were 73.11%, 88.46%, and 95.49%, corresponding to HG, 1PAN–HG, and 2PAN–HG. The influence of PAN–HG on the corrosion protection of the polyurethane coating applied on the CT3 steel was investigated. As a result, the PU containing 0.5% of 2PAN–HG showed the most effective protection of the CT3 steel substrate. The R_C of the coating was about 1.61×10^7 Ω cm^2, and after immersion for 30 days, the R_C value was 0.17×10^6 Ω cm^2. From all the analyzed results, PAN–HG has enhanced the corrosion protection and a complicated protection mechanism was also concluded and explained.

Received 17th June 2021
Accepted 6th September 2021

DOI: 10.1039/d1ra04683g

rsc.li/rsc-advances

Introduction

In recent years, metal corrosion causes damage in various fields, such as in transportation (*e.g.*, automobiles, aircrafts, ships), infrastructure (*e.g.*, pipelines, bridges, buildings) and industrial manufacturing (*e.g.*, oil-shore, production machine). Corrosion inhibition is the most effective solution, and has been studied continuously with various materials and agents. Many compounds are toxic or not entirely harmless/environmentally-friendly. Therefore, new anticorrosion agents are necessary, which have the same efficient (but less harmful) heavy metals (*e.g.*, Pb, Cr(VI), Cd, Ni).[1–3] Green corrosion inhibitors are worthy candidates because they have high efficiency, and are less or not harmful to the environment or human beings.[4–8] Green corrosion inhibitors are biodegradable and naturally-occurring substances. According to their chemical nature, they can be classified into two broad categories: organic green inhibitors and inorganic green inhibitors. Some organic green inhibitors are amino acids, polymers and biopolymers, surfactants, plant extracts, chemical medicines and ionic liquids. Inorganic green inhibitors are rare earth elements and clays or minerals. Here, we are interested in the combination of both inorganic and organic green inhibitors to improve the anticorrosion efficiency. Specifically, polyaniline was used as an organic green inhibitor and the hydrotalcite–graphene oxide hybrid was used as an inorganic green inhibitor.

Hydrotalcite (HT), a kind of double-layered hydroxide, is one of the inorganic mineral groups. HT is evaluated as an environmentally friendly material, and also a green inhibitor. HT is used as a layer coated on metal surfaces,[4–6] or as an additive in the organic coating. HT has been modified to improve polarity, as well as to increase dispersibility in the coating to achieve a uniform coating. Moreover, the modified HTs have high adsorption capacity, which helps to intercalate the more inhibitor molecules to their structure. When used, the inhibitor's molecules will be released into the coating to inhibit corrosion.[7–11] The vanadate ion has been intercalated into the double-layered structure of HT *via* an anion exchange mechanism, and HT–V was then used in an organic coating to protect the aluminium alloy.[16] The inhibitive effect of HT–V can be compared with highly effective chromate inhibitors. The result of the salt spray test on Al alloy coated epoxy-containing HT–V shows that the inhibitive efficiency was maintained after 1000 hours exposure in salt fog.

[a]*Institute of Chemical Technology, Vietnam Academy of Science and Technology, 1A TL29, Thanh Loc Ward, District 12, Ho Chi Minh City, Vietnam. E-mail: tban@ict.vast.vn*

[b]*Institute of Tropical Technology, Vietnam Academy of Science and Technology, 18 Hoang Quoc Viet, Cau Giay, Hanoi, Vietnam*

[c]*Graduate University of Science and Technology, 18 Hoang Quoc Viet, Cau Giay, Hanoi, Vietnam*

To enhance the inhibitory efficiency, HT has also been studied in fabricating a hybrid material or nanocomposite with graphene oxide (GO) because of the high barrier behavior of graphene oxide.[12–16] The preparation method of the nanocomposite from graphene oxide–hydrotalcite (GO–HT) has been investigated for fabrication,[21] wherein the membrane was used as nanofiltration for water desalination,[17,18] and co-precipitating HT in the presence of GO. It has been used as a corrosion inhibitor,[13,19,20] for gas adsorption,[21–23] water pollution treatment,[24,25] catalyst[26–28,32,33] and energy applications.[29–31] An inorganic film of GO–HT was successfully coated on the aluminium alloy 6N01 surface, and showed the perfect barrier against the permeation of H_2O, O_2 and Cl^-.[17] Similar to HT, GO–HT can be modified with appropriate anion and organic derivatives to improve the anticorrosion efficiency. GO–HT was also used as an anticorrosion filler in organic coatings, such as polyvinyl alcohol, PMMA, and acrylic film.[20,37–39] These research studies all proposed the same anticorrosion mechanism of GO–HT in organic coating, which is the enhancement of the barrier behavior.

Polyaniline (PAN) is a conducting polymer, and it has recently gained great efficiency in anticorrosion application because PAN has a complex anti-corrosion mechanism, including anodic protection,[40,41] cathodic protection,[42,63,64] controllable inhibitor release,[43–49] and barrier behavior.[49] PAN was widely used in various resins, such as epoxy, alkyd, acrylic, and efficiency.[49–51] When doping with camphor sulphonate, phenyl phosphonate and iodine, the doped PAN gives a double protection effect.[49,58] At first, the redox reaction that occurs between Fe and PAN leads to the reduction of PAN and the release of the doped anion. Then, the combination of the Fe cation and reduced PAN can give a passively complex layer to prevent the penetration of ions. Moreover, PAN was studied to fabricate a composite with either organic compounds, such as sulfonated chitosan,[52] 2-mercaptobenzothiazole,[53] benzoate,[69] nylon 66,[54] and palm oil;[55] or inorganic clays, such as magnetite clay, aluminium oxide and gamma-alumina.[24,34,56] All of those studies show that composites from PAN give good anti-corrosion performance in both HCl and NaCl environments.

In general, the most common anti-corrosion mechanism of GO–HT is the high barrier ability, while PAN supports both anode and cathode protection mechanisms. The hybrid material from GO–HT, as well as the nanocomposite/composite from PAN were widely studied for use as either corrosion inhibitors or used in the protective organic coating. However, there have not been any reports about the combination of PAN and GO–HT to produce a composite material that obtains an enhanced matrix mechanism of anti-corrosion.

Owing to the above advantages of GO, HT, and PAN, in this paper, we focused on a matrix from GO, HT, and PAN for a nanocomposite. HT was prepared using the co-precipitation method in the presence of GO to form a HG hybrid. Then, aniline was polymerized in the presence of HG *via* oxidation polymerization to produce the PAN–HG nanocomposite. The influence of PAN–HG on the anti-corrosion on carbon steel (CT3 steel) will also be investigated using the potentiodynamic polarization method, and then analyzed with a Tafel fit. PAN–HG was fabricated with various ratios of m_{PAN}/m_{HG} to investigate the influence of PAN on the anti-corrosion effect. In this paper, we fabricated 1PAN–HG and 2PAN–HG, which have ratios of $m_{PAN}/m_{HG} = 1/1$ and 2/1, respectively.

Results and discussion

Characterization of composite particles polyaniline–HG (PAN–HG)

Fourier transform IR (FT-IR). Chemical characterizations of HG, PAN, 1PAN–HG, and 2PAN–HG are shown in the FT-IR spectra (Fig. 1). GO was characterized by strong absorptions at 1716, 1616, 1384, and 1053 cm^{-1}, which were attributed to –C=O in the –COOH group, –C=C– in the benzene ring, –C–OH and –C–O–C–, respectively. In the FT-IR spectra of HG, there are blueshifts from 1716 cm^{-1} to 1562 cm^{-1} and from 1616 cm^{-1} to 1357 cm^{-1} because of the increase of bond length due to the interaction of GO and HT. Moreover, the bands at 767 and 609 cm^{-1} refer to the Zn–O and Al–O vibrations, which represent the basic lattice of HT.[57]

PAN presented with strong absorptions at 3443, 2939, 1515, 1481, 1288, 1130, and 875 cm^{-1}, which was evidence of the emeraldine form of PAN.[29,30] The band at around 3443 cm^{-1} was assigned to N–H stretching, and the band at around 2939 cm^{-1} was assigned to the aromatic C–H stretching. The characteristic stretching of the quinoid ring structure, and the band at 1481 cm^{-1} was attributed to both C=C and C–N of the benzenoid ring structure. All of these absorption peaks were characterized for the in-plane bending vibration. The band at around 1288 cm^{-1} indicated the vibration of the C–N stretching of the benzenoid ring, and the one at around 875 cm^{-1} was the C–H out-of-plane bending vibration parade-substituted benzene, indicating polyaniline formation.[59] In addition, the strong band at 1130 cm^{-1} was assigned to the C–H bending attached to the quinoid ring.

The PAN–HG composite represented the same characteristic bands as the pure PAN, and the corresponding bands of the PAN–HG composite were shifted to higher wavenumbers, which can be called a red-shift. This indicated that the 2D HT nanosheets affected the band positions in the FT-IR spectrum. The

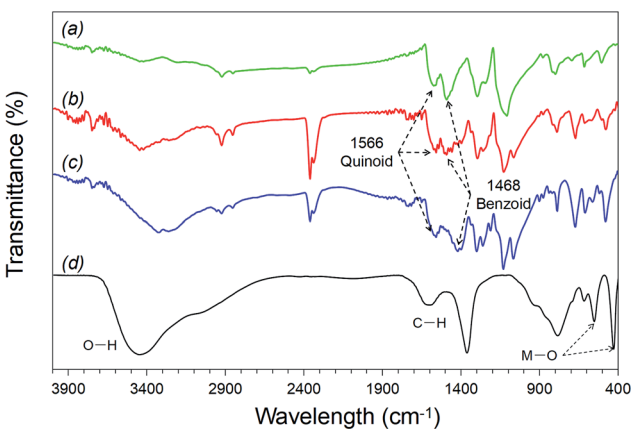

Fig. 1 FT-IR spectra of PAN (a), 2PAN–HG (b), 1PAN–HG (c) and HG (d).

C–N stretching band of quinoid at about 1515 cm^{-1} shifted to 1579 cm^{-1}, and the C=N stretching band at about 1481 cm^{-1} shifted to 1490 cm^{-1}. In contrast, the C–N stretching band of benzenoid at about 1288 cm^{-1} shifted to a lower wavelength band. These shifts in the spectrum indicated that the 2D HT nanosheets were attached to the PAN surface. It was due to the stretching of benzenoid and quinoid, which made the oscillation energy increase. On the other hand, the band at about 3236 cm^{-1} was assigned to the N–H hydrogen bond presented on the HG surface, which also confirmed the successful composite from GH with PAN.

X-ray diffraction. The crystal structures of HT, GO and HG were characterized by XRD (Fig. 2). The XRD pattern of GO exhibits a sharpened peak at $2\theta = 10.28°$, indicating the (0 0 1) plane. It also has a broad peak at a narrow angle of diffraction, which is from an amorphous structure ($2\theta = 2$–$5°$).

The composition of the material and the structure were determined by the XRD patterns, which are shown in Fig. 2. As the results show, the characteristic diffraction peaks of HG are the same as the diffraction peaks of HT and appear at 2θ of 11.70° (003), 23.56° (006), 34.58° (012), 39.56° (015), 46.78° (018), 60.26° (110), and 61.64° (113), which are attributed to the formation of nano-plates and the hydroxide layered structure combined with graphene oxide sheets. In the HT XRD pattern, there is a small amount of boehmite, which caused a decrease in the material crystallinity. Meanwhile, weak peaks of ZnO and bayerite were identified in the HG XRD pattern. The reason of this can come from the reduction reaction of Zn^{2+} with functional groups on the GO surface. This result shows that the HT crystals are stable and growing on the GO plates. At the same time, HT linked on the surface of larger GO plates will have diffraction coinciding with the surface diffraction (100) by GO.

$$d = (n \times \lambda)/(2 \times \sin\theta) \quad (1)$$

The Raman diagram of GO (Fig. 3) shows that there are 2 sharp peaks with strong intensity at 1346 cm^{-1}, 1588 cm^{-1}, and 1 peak with very weak intensity at 2700 cm^{-1}, which are characterized as the D peak, G peak, and 2D peak, respectively. The G peak is weaker than the D peak because the oxidation reaction attaching the polar functional groups on the GO surface from the initial bonds in the strong graphite lattice increases the number of C–sp^3 bonds compared to C–sp^2 bonds. The relative intensity ratio of the D peak to the G peak is I_D/I_G = 1.04, indicating that the graphite blocks have been stripped and oxidized to GO. The Raman diagram of the HG sample clearly shows the D peak and G peak in the range of 1596–1600 cm^{-1}, respectively. The relative intensity ratio of these two peaks increased, specifically $I_D/I_G = 1.30$, as a result of the reduction in the sp^2 bond size in the hexagonal structure of GO, structural defects in the GO network, as well as the reduction of O functional groups in the GO structure.[35,36] In addition, HG materials pose the full Raman scattering characteristics of HT materials in the region of 582 cm^{-1} and 1092–1116 cm^{-1}. These Raman scattering analysis results are in agreement with the published results of Xiaohu Luo[17] and Ningning Hong.[20]

The XRD pattern of PAN shows that it has two broad diffraction peaks at $2\theta = 20.28°$ and 26.84°, which are attributed to the periodicities parallel and perpendicular to the polymer chain, respectively. The XRD patterns of both 1PAN/HG and 2PAN/HG have broad diffraction peaks at around 20.28° and 26.84°, respectively, corresponding to the pure PAN. In these diffraction peaks, 2PAN/HG with the higher ratio of m_{PAN}/m_{HG} obtained stronger diffraction than 1PAN/HG. In addition, both 1PAN/HG and 2PAN/HG have diffractions at 36.34°, 37.85° and 58.79° corresponding to the left shift of the diffraction of HG at the (009), (015) and (110) planes, respectively. The XRD results clearly show that the PAN particles are not intercalated in the interlayer of HG, and the layered double hydroxide structure of HG is maintained (Fig. 4).

SEM images

The morphology of the material was observed by SEM images in Fig. 5. The morphology of HG still has GO plates, but with HT

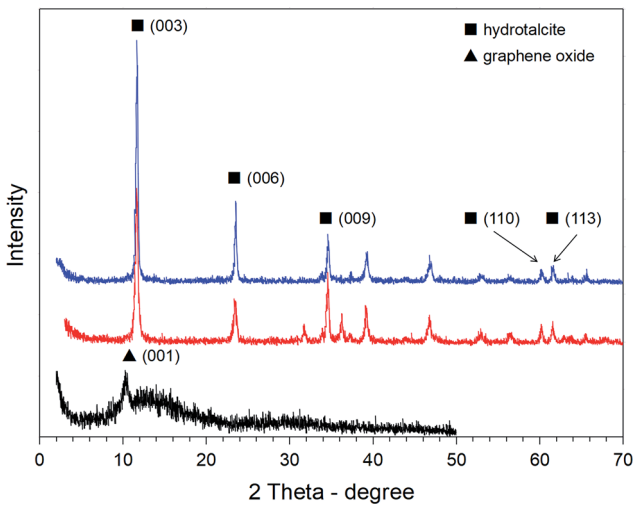

Fig. 2 XRD pattern of GO (a), G–HT (b) and HT (c).

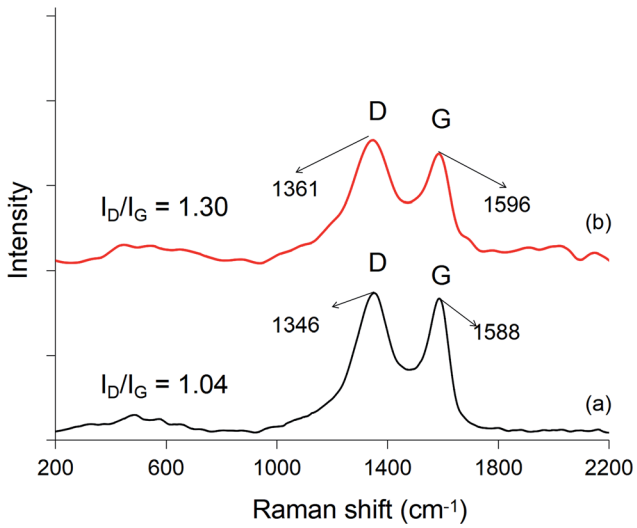

Fig. 3 Raman spectra of graphen oxide (GO) and hydrotalcite–GO hybrid (HG).

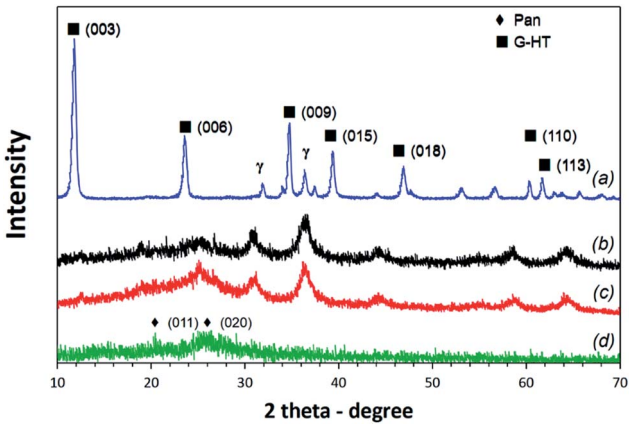

Fig. 4 XRD patterns of HG (a), 1PAN–HG (b), 2PAN–HG (c) and PAN (d).

crystals distributed on the surface. This helps the GO plates not be folded by the physical bonding. PAN has needle shape crystals due to the preparation method, which using tartaric acid as an orientation agent for crystal development. This is consistent with the publication of C. Muthuselvi *et al.*[60] The SEM image of PAN–HG shows that the nanoparticles of HG were attached to the PAN crystal. This result is completely consistent with the results of the structural analysis by the significantly reduced X-ray diffraction.

Corrosion protection composite

The passivation of CT3 steel in an electrochemical system with/without composite particles was examined using the potentiodynamic technique. The behavior of the potentiodynamic polarization curves for the CT3 steel surface (working electrode) indicates whether the CT3 steel surface is cathodically protected (sacrificial anode principle) or anodically protected (passivation principle).[61–66] The CT3 steel surface was exposed to a 3.5% NaCl aqueous solution and a series of 3.5% NaCl aqueous solutions containing 1% (wt/wt) GO, PAN, HG, 1PAN–HG, and 2PAN–HG, and were labeled GO–sol, PAN–sol, HG–sol, 1PAN–HG–sol, and 2PAN–HG–sol, respectively. All of the solutions in the electrochemical cells were magnetically stirred for 2 hours. Fig. 6 shows the potentiodynamic polarization curves and the kinetic parameters obtained after Tafel fitting using EC-LAB analyst version 10.36, and is also presented in Table 1.

Fig. 6a shows the Tafel plots of CT3 steel in 3.5% NaCl, GO–sol, and HG–sol. Fig. 6b shows the Tafel plots of CT3 steel in HG–sol, PAN–sol, 1PAN–HG–sol and 2PAN–HG–sol. The E_{corr} of CT3 steel in bare 3.5% NaCl solution was −802.24 mV. The presence of GO, HG, and composite particles caused the shift of E_{corr} to more positive values, which are −740.24 mV, −495.03 mV, −682.64 mV, −406.97 mV, and the highest is −381.99 mV, corresponding to GO–sol, HG–sol, PAN–sol, 1PAN–HG–sol, and 2PAN–HG–sol, respectively.

The corrosion current density (I_{corr}) is directly proportional to the corrosion rate at the point of intersection of the anodic and cathodic curves. In GO–sol, I_{corr} decreased to 6.24 μA cm^{-2} compared to NaCl–sol, which is 27.73 μA cm^{-2}. Thus, the corrosion protection reached 77.50%. The I_{corr} of HG–sol and PAN–sol are 7.77 and 6.32, respectively, which are lower than that for NaCl–sol, but higher than that of GO–sol due to the lower barrier ability of HG and electrical conductivity of PAN. As a result, the corrosion protections are 71.11% and 77.21%. The I_{corr} values of 1PAN–HG–sol and 2PAN–HG–sol have significantly decreased to 0.92 and 0.36, respectively, corresponding to the corrosion protection of 88.46% and 95.49%. The presence of PAN in the structure of the composite PAN–HG helps to enhance the protection on the CT3 steel surface due to the complicated protection mechanism of PAN. Those mechanisms

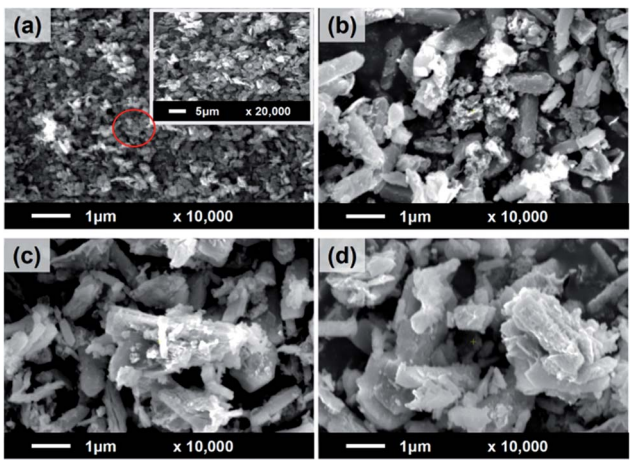

Fig. 5 SEM images of HG (a), PAN (b), 1PAN-HG (c) and 2PAN-HG (d).

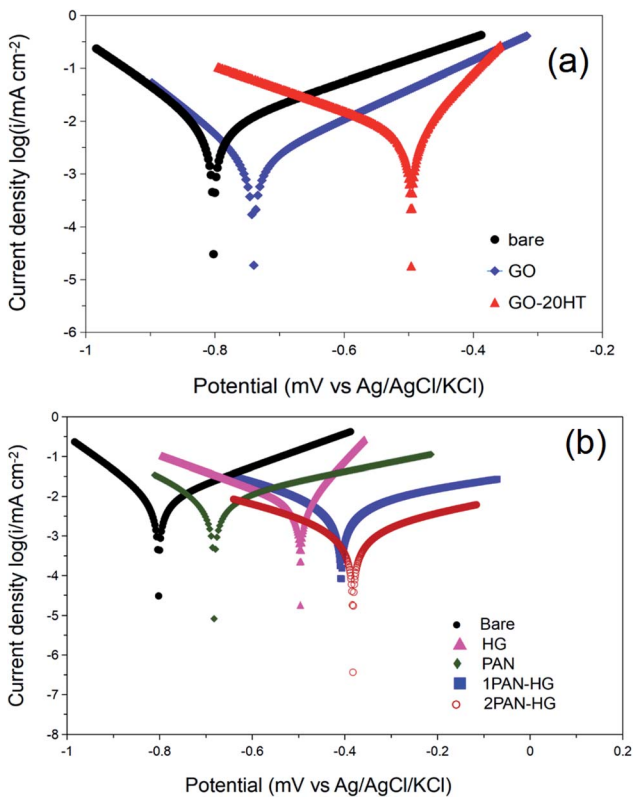

Fig. 6 Potentiodynamic polarization curves of CT3 steel in 3.5% NaCl solution without/with GO, HG, PAN, 1PAN–HG and 2PAN–HG.

Table 1 Tafel fitting results from the potentiopolarization curves

Sample	E_{corr}, mV *vs.* Ag/AgCl/KCl	I_{corr}, μA cm^{-2}	b_a, mV dec^{-1}	$-b_c$, mV dec^{-1}	R_{corr}, mm year^{-1}	η, (%)
Bare CT3	−802.24	27.73	123.4	240.1	52.33	—
GO	−740.24	6.24	179.5	106.6	11.78	77.50
HG	−495.03	7.77	60.6	165.0	14.64	73.11
PAN	−682.64	6.32	123.0	80.0	10.33	77.21
1PAN–HG	−406.97	3.20	160.5	189.4	0.02	88.46
2PAN–HG	−381.99	1.25	273.1	318.1	0.84	95.49

are anodic protection,[45–50] cathodic protection,[50–53] controlled inhibitor release,[54–56] and barrier protection.[72]

From the results of corrosion protection, both 1PAN–HG and 2PAN–HG have the same corrosion protection. So, both of them will be combined in the PU coating, and investigated for anti-corrosion organic coating.

Characterization of anti-corrosion coatings

The PU coatings containing HG, 1PAN–HG, and 2PAN–HG were fabricated on a well prepared CT3 steel surface and labeled PU(HG), PU(1PAN–HG), and PU(2PAN–HG), respectively.

The microstructure and dispersion of composite particles in the PU coating were observed by SEM images in Fig. 7. The SEM images show that both HG, 1PAN–HG, and 2PAN–HG are well dispersed in the PU coating, and that will help increase the protective effect of the PU coating.

On the other hand, the presence of PAN causes the increase in the contact angle of the PU coating surface. This helps in increasing the barrier property of the coating, and constrains the diffusion of water into the coating. The diagram in Fig. 8 shows the contact angle dropwise on the surface of PU(HG), PU(1PAN–HG), and PU(2PAN–HG), which are 80.8°, 103.9°, and 107.1°. Therefore, PU(2PAN–HG) was predicted to be the most anti-corrosion effective, and the electrochemical analysis results will be discussed.

In this research, the EIS results obtained from the PU coating containing HG, 1PAN–HG, and 2PAN–HG after 1, 5, 10, and 30 days immersion in 3.5% NaCl solution are shown in Fig. 10.

The changes in the protection performance of the coatings can also be illustrated by Nyquist plots. After 1 day immersion, the Nyquist plots of PU(2PAN–HG) show a one-time constant with only one arc, while Nyquist plots of PU(HG) and PU(1PAN–HG) have more than one arc. The corrosive medium did not reach the metal surface because of the high barrier of PU(2PAN–HG), which was proved by the contact angle of the dropwise coating surface.[73] After 5 days, 10 days, and 30 days, all Nyquist plots of PU(HG), PU(1PAN–HG), and PU(2PAN–HG) have more than one arc because the corrosive medium diffused through the coating and reached the metal surface, so that corrosion has occurred. The electrical equivalent circuit shown in Fig. 9 was employed to fit the EIS data using the software EC-LAB version 10.36. R_S, R_C, and R_{CT} represent the electrolyte resistance, the coating resistance, and the charge transfer resistance, respectively. The CPE_C and CPE_{dl} are related to the constant phase element of the coating capacitance and double layer due to the dispersion effect.

Nyquist plots illustrate the changes in the protection performance of the coatings. As the results from Table 2 show, the R_C of PU(HG) has slightly increased in the short immersion period. The R_C after 1 day immersion is 3.50×10^6 Ω cm^2, and then it increases to 3.96×10^6 Ω cm^2 after 5 days immersion. It is due to the anticorrosion mechanism of HG, which is explained as the ion exchangeable hydrotalcite to trap Cl^-, as well as electron trapping of graphene to reduce the erosion of the medium.[74] However, Cl^- ion exchange and electron trapping of HG have limited capability. Therefore, the R_C of PU(HG) decreased to 1.91×10^3 Ω cm^2, and then 0.40×10^3 Ω cm^2 after 20 days and 30 days, respectively.

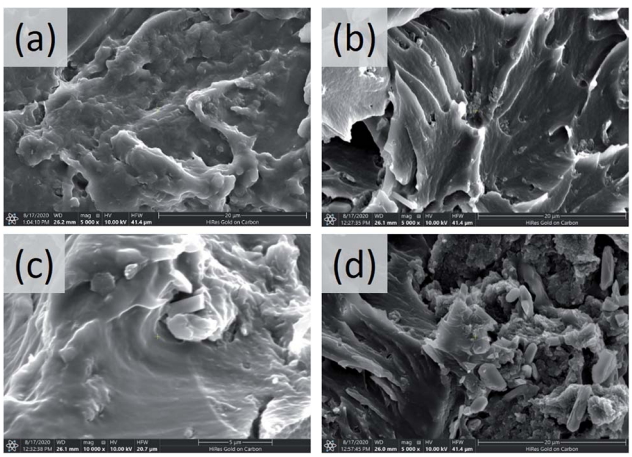

Fig. 7 Microstructure of PU (a), PU(HG) (b), PU(1PAN–HG) (c), and PU(2PAN–HG) (d) observed from SEM images.

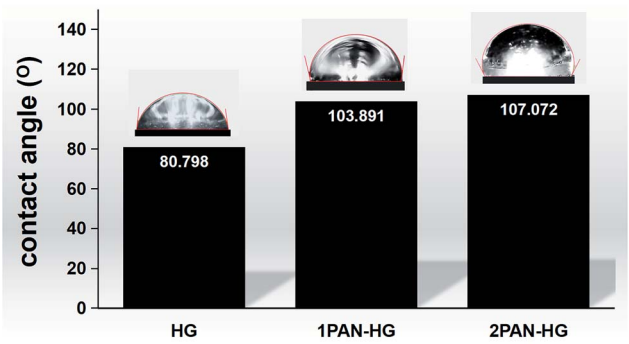

Fig. 8 Contact angle of water dropwise on the PU(HG), PU(1PAN–HG) and PU(2PAN–HG) coating surfaces.

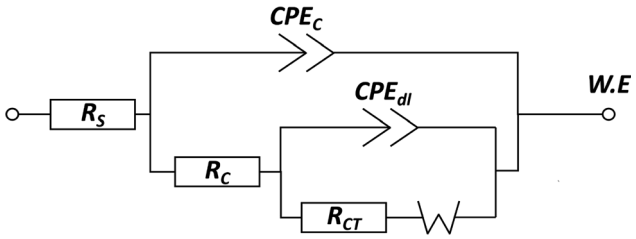

Fig. 9 Equivalent electrical circuit used for EIS fitting.

PU(1PAN–HG) and PU(2PAN–HG) have higher R_C and are more stable than PU(HG) because of the anti-corrosion mechanism of PAN. The R_C of PU(1PAN–HG) and PU(2PAN–HG) are not much different after 1 day of immersion. The R_C of PU(1PAN–HG) has decreased in turn from 1.15×10^7, 1.08×10^6, 7.98×10^5, and 4.61×10^4, corresponding to 1, 5, 10, and 30 days of immersion. For the PU(2PAN–HG), the R_C has slightly decreased in turn from 1.61×10^7, 8.85×10^6, 4.62×10^6, and 0.17×10^6 Ω cm^2, corresponding to 1, 5, 10 and 20 days of immersion.

All the Nyquist and Bode plots show one-time constant behavior, revealing that only charger transfer resistance is present in the electrochemical cell. In the Bode plots, the values of Z' and Z'' represent the real and imaginary components of impedance in the correlated relationship of $|Z| = \sqrt{Z'^2 + Z''^2}$. Moreover, the value of $|Z|$ determined from the Bode plots at low frequency (0.01 Hz) can be regarded as a reference to assess the protection

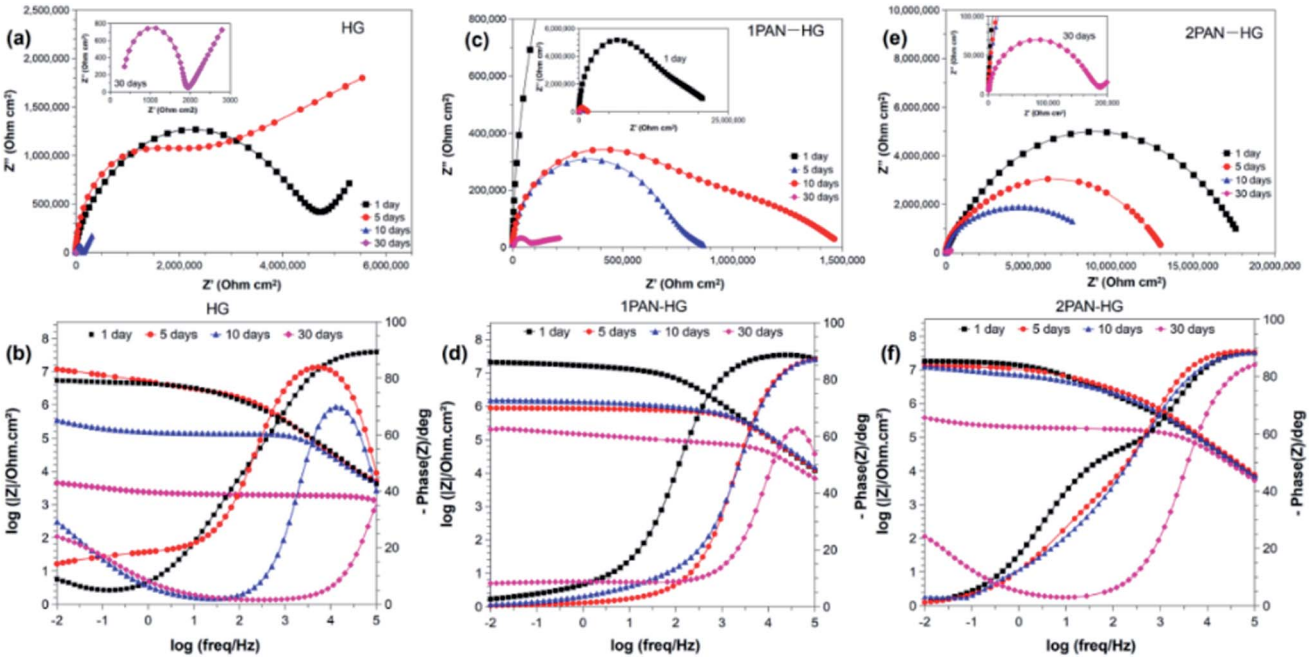

Fig. 10 Nyquist plots and Bode plots of PU(HG) (a and d), PU(1PAN–HG) (b and e) and PU(2PAN–HG) (c and f) immersed in 3.5% NaCl solution for different times.

Table 2 EIS fitting results from Nyquist and Bode plots of PU(HG), PU(1PAN–HA) and PU(2PAN–HG) immersed in 3.5% NaCl solution in various times

			CPE_{coat}			CPE_{dl}			
Sample	Time	R_S, Ω cm^2	Q_C, F s^n·cm^{-2}	n	R_C, Ω cm^2	Q_C, F s^n·cm^{-2}	n	R_{CT}, Ω cm^2	s, Ω s$^{-1/2}$
HG	1 day	120.24	1.22×10^{-9}	0.897	3.50×10^6	1.34×10^{-8}	0.352	12.75	37.38
	5 days	195.64	4.36×10^{-9}	0.798	3.96×10^6	2.26×10^{-8}	0.279	1.37×10^5	1.09×10^5
	10 days	228.81	1.84×10^{-8}	0.770	1.91×10^3	1.42×10^{-3}	0.878	32.34	0.92×10^3
	30 days	220.74	2.06×10^{-9}	0.841	0.40×10^3	1.21×10^{-7}	0.407	1.29×10^3	0.33×10^3
1PAN–HG	1 day	165.05	40.0×10^{-9}	0.928	1.15×10^7	1.59×10^{-5}	0.631	1.39×10^7	58
	5 days	185.88	1.23×10^{-9}	0.810	1.08×10^6	1.87×10^{-11}	0.464	7.97×10^4	6.93×10^4
	10 days	204.77	4.10×10^{-9}	0.725	7.98×10^5	1.77×10^{-7}	0.510	5.78×10^5	3.00×10^4
	30 days	200.19	1.43×10^{-9}	0.896	4.61×10^4	5.68×10^{-6}	0.409	4.63×10^5	19.98
2PAN–HG	1 day	163.45	2.35×10^{-9}	0.825	1.61×10^7	5.22×10^{-4}	0.304	1.28×10^6	2.80
	5 days	177.70	3.62×10^{-9}	0.750	8.85×10^6	1.63×10^{-7}	0.715	1.36×10^3	0.11×10^3
	10 days	199.73	2.51×10^{-9}	0.790	4.62×10^6	1.06×10^{-7}	0.530	4.92×10^6	50
	30 days	201.51	1.18×10^{-9}	0.888	0.17×10^6	2.57×10^{-7}	0.40	2.51×10^3	2.68×10^3

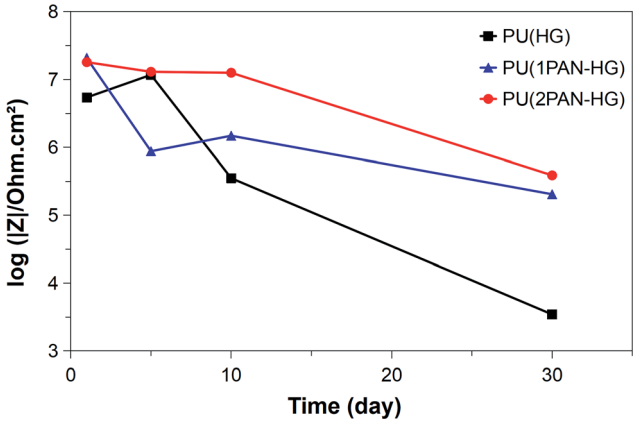

Fig. 11 $|Z|_{f=0.01\ Hz}$ values of PU(HG), PU(1PAN–HG) and PU(2PAN–HG) immersed in 3.5% NaCl solution in different times.

performance of the coatings. Fig. 11 shows the trend of the $|Z|_{f=0.01\ Hz}$ values of PU(HG), PU(1PAN–HG), and PU(2PAN–HG). $|Z|_{f=0.01\ Hz}$ of PU(HG) has increased from $5.43 \times 10^6\ \Omega\ cm^2$ to $11.70 \times 10^6\ \Omega\ cm^2$ after immersion in 3.5% NaCl solution for 5 days due to the feature of HG. Then, this value has decreased to $0.35 \times 10^6\ \Omega\ cm^2$ and $3.45 \times 10^3\ \Omega\ cm^2$ after 10 and 30 days, respectively. The $|Z|_{f=0.01\ Hz}$ values of PU(1PAN–HG) and PU(2PAN–HG) are enhanced compared with PU(HG). After 1 day immersion, $|Z|_{f=0.01\ Hz}$ is $2.07 \times 10^7\ \Omega\ cm^2$ for PU(1PAN–HG) and $1.80 \times 10^7\ \Omega\ cm^2$ for PU(2PAN–HG). After 30 days immersion, these values have decreased to $2.03 \times 10^4\ \Omega\ cm^2$ for PU(1PAN–HG) and $3.87 \times 10^4\ \Omega\ cm^2$ for PU(2PAN–HG).

The results show that PAN played an important role in enhancing the corrosion resistance of the PU coating based on the complicated protection mechanism. That is the combination of the physical barrier mechanism, controlled inhibitor release mechanism,[43,47,71] cathodic protection mechanism, and the most important is the anodic protection mechanism. For the anodic protection mechanism, reactions eqn (2) and eqn (3) show that the reduction of PAN happened in the passivation of the metal substrate, whereas the oxidized form of PAN can be recovered by

$$1/nM + 1/mPAN\text{-}ES^{m+} + y/nH_2O \rightarrow 1/nM(OH)y^{(n-y)+} + 1/mPAN\text{-}LEB^0 + y/nH^+ \quad (2)$$

$$m/4O_2 + m/2H_2O + PAN\text{-}LEB^0 \rightarrow PAN\text{-}EB^{m+} + mOH^- \quad (3)$$

The reduction of oxygen to hydroxide ions shifts from the metal surface to the PAN electrolyte interface, associated perhaps with reaction eqn (4):

$$m/4O_2 + m/2H_2O + me^- \rightarrow mOH^- \quad (4)$$

Corrosion protective mechanism

From the above observations and analysis, the anticorrosion mechanisms of the PU coating containing HG, 1PAN–HG, and 2PAN–HG are proposed in Fig. 12. It can be discussed from different aspects as mentioned below.

First, either GO or PAN has a protective barrier mechanism, which can extend the diffusion path of the electrolyte and reduce the e^- diffusion rate from the environment to the steel substrate. Meanwhile, GO has a large and flexible sheet structure that produces the best physical protective barrier, the barrier mechanism of PAN is more complicated. The presence of solid micro/nanofillers in the organic coating exhibits better corrosion protection due primarily to:

- Stability of the redox activity of PAN and diminution of its degradation as the reaction eqn (5);

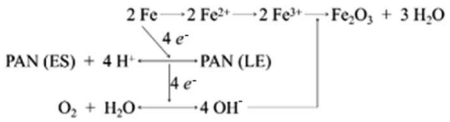

(5)

- The uniform distribution of PAN and the increased possibility of forming uniform passive layers on the metal surface.
- The restriction of penetration and lengthening of the diffusion path of water and oxygen molecules through the nanocomposite coating.

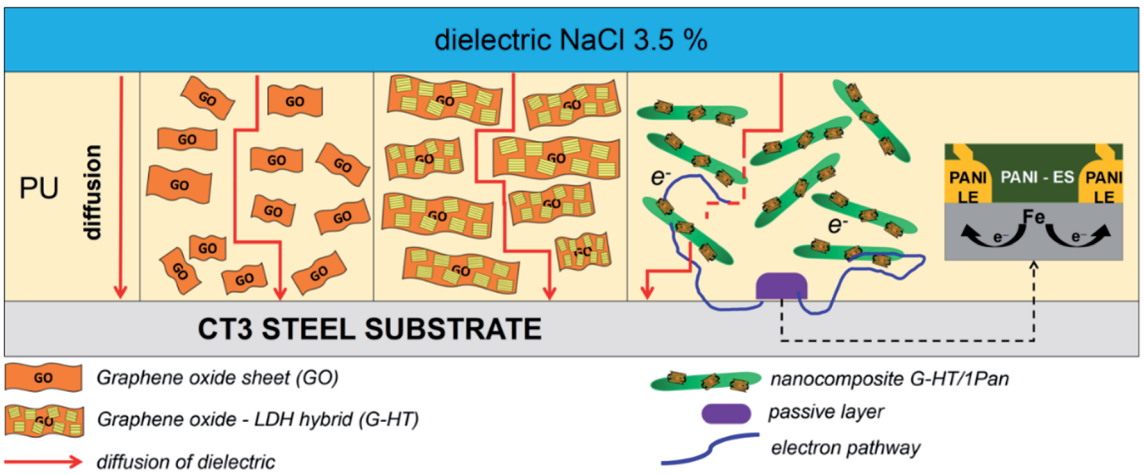

Fig. 12 Corrosion protection mechanism of GO, HG and PAN–HG.

- The ion-exchangeability of both HG and PAN can help to trap the anion Cl^- and control the corrosion rate.

- The ability of trapping e^- in the structure of HG that helps to reduce the corrosion rate.

- The enhancement of mechanical stability of the coating and its high adhesion strength to the metal substrate.

In addition, the corrosion protection of PAN–HG is mostly because of the anodic protection mechanism of PAN. The PU(PAN–HG) coating protects the steel due to both barrier and blocking ability of the nanocomposite. That reaction is the conversion reaction of PAN when receiving e^- and transforms from the ES to LS state. The PAN–LS layer at the contact surface of the paint-substrate will convert from the LS to ES state.[47,49,50,67,68,70] So that, after forming the surface passivation layer, electrons are continuously transferred to the external environment, thereby inhibiting the corrosion reaction occurring.[72]

Moreover, HG and PAN–HG can control the corrosion reaction rate due to the ion-exchangeability of both PAN and HG. Therefore, Cl^- from the diffusion of the electrolyte and e^- generated from the corrosion reaction on the metal surface can be trapped in the structure of HG and especially PAN, where a redox reaction of PAN will occur and cause the anodic protection mechanism.

Experimental

Materials

All chemicals used in this research, such as graphite, $KMnO_4$, $Zn(NO_3)_2 \cdot 6H_2O$, $Al(NO_3)_3 \cdot 9H_2O$, ammonium persulphate (APS), aniline, and tartaric acid (TA) were synthesis grade and purchased from MERCK. For the preparation of the polyurethane coatings, polyacrylate as the base and polyisocyanate as the hardener were obtained from Nippon Polyurethane Industry.

Synthesis composite from polyaniline with HG hybrid (PAN–HG). Graphene oxide (GO) was prepared using the Hummers' method, as previously described.[75] The hybrid from GO and hydrotalcite was synthesized *via* coprecipitation of a mixture of zinc nitrate and aluminum nitrate in the presence of GO and was labeled HG. In detail, 6.8 g of $Zn(NO_3)_2 \cdot 6H_2O$ and 13.6 g of $Al(NO_3)_3 \cdot 9H_2O$ were dissolved in 50 ml deionized water. 0.5 g of GO was dispersed in 100 ml deionized water, and the GO solution was sonicated at 400 kHz for about 1 hour and then vigorously stirred magnetically for about 30 minutes. The mixture of zinc–aluminum salt was dropped into the GO solution for co-precipitation. The pH of co-precipitation was controlled at a value of 9.5–10 using 0.2 M NaOH. The suspension was centrifuged and washed with distilled water until neutralized. HG was then vacuum dried at 50 °C for 6 hours.

50 mg of HG was dispersed in 50 ml of ethanol and sonicated for 2 hours, then vigorously stirred magnetically for about 30 minutes in an ice bath. Aniline was dissolved in 25 ml of 0.5 M TA solution and APS was dissolved in the remaining 25 ml of 0.5 M TA solution. The monomer solution was added dropwise into HG suspension for absorption. Then, the APS solution was added dropwise into the reaction for the polymerization of aniline. The mixture changed from light yellow to blue, and finally turned to a dark green solution. The polymerization was kept in an ice bath at 2–4 °C for 12 hours. Then, the composite particles were washed with a mixture of ethanol : deionized water (50 : 50). The product was then dried in vacuum at 60 °C for 6 hours.

Preparation of PU coating containing composite PAN–HG. HG, 1PAN–HG, and 2PAN–HG were ground well and then dispersed in PU resin at 0.5 wt% mass loading (0.05 g) using sonification, and then ultraspeed homogenized at 13 000 rpm. Then, the hardener was added to resin mixtures under high-speed stirring. The coatings were applied on CT3 steel plates, which were surface pre-treated well and dried at room temperature for 48 hours. The thickness of the coating was 10 ± 0.02 μm.

Characterization of the composites. The Fourier transform infrared (FT-IR) spectra of the HG hybrid, 1PAN–HG, and 2PAN–HG composites were obtained using the KBr method on a Bruker Tensor 27 spectrometer, operated in the 400–4000 cm^{-1} region at 2 cm^{-1} resolution and for 32 scans.

Powder X-ray diffraction patterns of the HG hybrid, 1PAN–HG, and 2PAN–HG composites were obtained using a Bruker D8 Advance diffractometer with Cu Kα radiation (1.5406 Å) at room temperature under atmospheric pressure. Data were collected in the 2 theta range of 5–70° with a step size of 0.02° and a scanning rate of 1° min^{-1}.

The Raman spectra of GO and HG were recorded by Lab SPEC from HORIBA with the Raman shift range of 0–4000 cm^{-1}, and using a laser at 532 nm.

The HG hybrid, 1PAN–HG, and 2PAN–HG composites and the coating structure at the cross-sections of PU(HG), PU(1PAN–HG), and PU(2PAN–HG) were observed by scanning electron microscopy (SEM). SEM observations were carried out using a Thermo Scientific E-SEM instrument.

Electrochemical characterization. The electrochemical measurements were monitored with an AUTO LAB, PGS-stat potentiostat by using a three-electrode cell. The potentiodynamic polarization and electrochemical impedance spectroscopy (EIS) curves were measured in 3.5% NaCl solution at room temperature. For both measurements, an (Ag/AgCl, saturated KCl) electrode was used as the reference electrode (Ag/AgCl, saturated KCl), and a platinum mesh panel of 2.0 cm × 8.0 cm was used as the counter electrode. Before testing, the working electrode was maintained at its open circuit potential (OCP) for 15 minutes until the OCP reached a steady state.

The potentiodynamic polarization measurement was composed of CT3 steel with an exposed area of 0.5024 cm^2 as the working electrode. For evaluation of the corrosion inhibition effect, an accurate amount of HG hybrid, 1PAN–HG, and 2PAN–HG was dispersed in 50 ml of 3.5% NaCl as the electrolyte. The working electrode was immersed in the electrolyte with/without containing materials for 2 hours. The corrosion inhibition effect was studied by using potentiodynamic polarization curves with a 0.5 mV of potential scan rate, and started from a potential of −0.03 V to 0.03 *vs.* OCP.

For the EIS measurement, the various PU coatings containing HG, 1PAN–HG, and 2PAN–HG fabricated on the CT3 steel surface were used as working electrodes with an exposed area of

5.723 cm^2. The frequency scanning was 100 kHz to 10 mHz with an amplitude of 10 mV.

Then, all potentiodynamic polarization curves and electrical impedance spectra were calculated using Tafel fitting, Nyquist, and Bode fitting by EC-LAB version 10.36 software. The corrosion protection performance was determined by the corrosion current density (i_{corr}) and corrosion potential (E_{corr}), and the protection efficiency (η) was calculated by eqn (6) below.

$$\eta\ (\%) = \frac{i_{corr}(\text{bare}) - i_{corr}(\text{cp})}{i_{corr}(\text{bare})} \times 100 \quad (6)$$

where i_{corr}(bare) and i_{corr}(cp) are corrosion current densities of the CT3 steel electrode in 3.5% NaCl solution without/with composite particles.

Conclusions

In this research, composite PAN–HG was completely prepared using directed polymerization of polyaniline on HG. The results indicated the layer structure of HG is still maintained and attached to the PAN crystal surface with a strong bond between those particles. The electrochemical properties of these composites were evaluated by potential polarization curves. Then, the results were calculated with Tafel fitting to give the effective corrosion protection at 73.11%, 88.46%, and 95.49%, corresponding to HG, 1PAN–HG, and 2PAN–HG, respectively. The PU coating samples was prepared with 1% content of HG, 1PAN–HG, and 2PAN–HG. The corrosion protection abilities of the coating samples were evaluated using the EIS method. As a result, the PU(2PAN–HG) coating shows the most effective protection of the CT3 steel substrate with the R_C of the coating after 1 day immersed in 3.5% NaCl solution at about 1.61×10^7 Ω cm^2. After 30 days of immersion, the R_C value was 0.17×10^6 Ω cm^2. In addition, the mechanism of the corrosion protection was explained as the combination of both barrier mechanism of HG and PAN, ion-exchange mechanism to trap the Cl^- and control the corrosion rate, the ability to trap e^- in the structure of HG and the most noticeable is anodic protection mechanism coming from PAN. This helps to make the enhancement of the corrosion protection ability of PAN–HG compared with HG.

Author contributions

Boi An Tran: Corresponding author, Conceptualization, Investigation, Writing-Original Draft, Writing-Review & Editing. Huynh Thanh Linh Duong: Investigating, Editing. Thanh Thao Phan: Science Advisor, Writing-Review. Thi Xuan Hang To: Science Advisor, Writing-Review.

Conflicts of interest

There are no conflicts to declare.

Acknowledgements

The authors would like to thank Dr Thanh Thao Phan and Dr Thi Xuan Hang To for their science and technical assistance, and the Institute of Chemical Technology for their analysis equipment support.

Notes and references

1 X. Zhang, *et al.*, Characterization of chromate conversion coatings on zinc using XPS and SKPFM, *Surf. Coat. Technol.*, 2005, **197**, 168–176.
2 N. M. Ahmed, M. G. Mohamed, M. R. Mabrouk and A. A. ELShami, Novel anticorrosive pigments based on waste material for corrosion protection of reinforced concrete steel, *Constr. Build. Mater.*, 2015, **98**, 388–396.
3 M. Svoboda and J. Mleziva, Properties of coatings determined by anticorrosive pigments, *Prog. Org. Coat.*, 1984, **12**, 251–297.
4 A. A. Al-Amiery, F. A. Binti Kassim, A. A. H. Kadhum and A. B. Mohamad, Synthesis and characterization of a novel eco-friendly corrosion inhibition for mild steel in 1 M hydrochloric acid, *Sci. Rep.*, 2016, **6**, 19890.
5 C. J. Prabha, S. Sadagopan and G. Venkatachari, Polyaniline as corrosion inhibitor for iron in acid solutions, *J. Appl. Polym. Sci.*, 2006, **101**, 2144–2153.
6 U. Bharatiya, P. Gal, A. Agrawal, M. Shah and A. Sircar, Effect of Corrosion on Crude Oil and Natural Gas Pipeline with Emphasis on Prevention by Ecofriendly Corrosion Inhibitors: A Comprehensive Review, *J. Bio- Tribo-Corrosion*, 2019, **5**(35), 1–12.
7 A. Rubaye, H. Abdulsahib and A. Abdulrazzaq Abdulwahid, Corrosion Inhibition Properties of Norepinephrine Molecules on Mild Steel in Acidic Media, *J. Encapsulation Adsorpt. Sci.*, 2015, **5**, 155–164.
8 Y. Kadri, E. Srasra, I. Bekri-Abbes and P. Herrasti, Facile and eco-friendly synthesis of polyaniline/ZnO composites for corrosion protection of AA-2024 aluminium alloy, *J. Electroanal. Chem.*, 2021, **893**, 115335.
9 M. Iqbal, L. Sun, A. Barrett and M. Fedel, Layered Double Hydroxide Protective Films Developed on Aluminum and Aluminum Alloys: Synthetic Methods and Anti-Corrosion Mechanisms, *Coatings*, 2020, **10**, 428.
10 W. Zhang and R. G. Buchheit, Hydrotalcite Coating Formation on Al-Cu-Mg Alloys from Oxidizing Bath Chemistries, *Corrosion*, 2002, **58**, 591–600.
11 K. Katagiri, Y. Goto, M. Nozawa and K. Koumoto, Preparation of layered double hydroxide coating films via the aqueous solution process using binary oxide gel films as precursor, *J. Ceram. Soc. Jpn.*, 2009, **117**, 356–358.
12 D. N. Thuy, H. T. T. Xuan, A. Nicolay, Y. Paint and M.-G. Olivier, Corrosion protection of carbon steel by solvent free epoxy coating containing hydrotalcites intercalated with different organic corrosion inhibitors, *Prog. Org. Coat.*, 2016, **101**, 331–341.
13 D. Li, *et al.*, Anticorrosion organic coating with layered double hydroxide loaded with corrosion inhibitor of tungstate, *Prog. Org. Coat.*, 2011, **71**, 302–309.
14 A. Seniski, R. F. Monteiro, G. T. Carrera, M. D. O. G. P. Bragança and K. F. Portella, The inhibitory and comparative effects of Zn-Al layered double hydroxide

microcontainers intercalated with benzotriazole and nitrite for corrosion protection coatings on AISI 1010 carbon steel, *Matéria*, 2020, **25**(2), 1–10.

15 J. Rodriguez, *et al.*, Incorporation of layered double hydroxides modified with benzotriazole into an epoxy resin for the corrosion protection of Zn-Mg coated steel, *Prog. Org. Coat.*, 2020, **149**, 105894.

16 S. P. V. Mahajanam, *Application of hydrotalcite as corrosion inhibiting pigment in organic coating*, 2005.

17 X. Luo, *et al.*, Synthesis and Enhanced Corrosion Protection Performance of Reduced Graphene Oxide Nanosheet/ZnAl Layered Double Hydroxide Composite Films by Hydrothermal Continuous Flow Method, *ACS Appl. Mater. Interfaces*, 2017, **9**, 18263–18275.

18 L. Yan, M. Zhou, X. Pang and K. Gao, One-Step In Situ Synthesis of Reduced Graphene Oxide/Zn–Al Layered Double Hydroxide Film for Enhanced Corrosion Protection of Magnesium Alloys, *Langmuir*, 2019, **35**, 6312–6320.

19 Y.-X. Yan, *et al.*, Micrometer-Thick Graphene Oxide–Layered Double Hydroxide Nacre-Inspired Coatings and Their Properties, *Small*, 2016, **12**, 745–755.

20 N. Hong, *et al.*, Co-precipitation synthesis of reduced graphene oxide/NiAl-layered double hydroxide hybrid and its application in flame retarding poly(methyl methacrylate), *Mater. Res. Bull.*, 2014, **49**, 657–664.

21 F. Wang, *et al.*, One-step synthesis of nickle iron-layered double hydroxide/reduced graphene oxide/carbon nanofibres composite as electrode materials for asymmetric supercapacitor, *Sci. Rep.*, 2018, **8**, 8908.

22 X. Wang, *et al.*, Hydrotalcite/graphene oxide hybrid nanosheets functionalized nanofiltration membrane for desalination, *Desalination*, 2019, **451**, 209–218.

23 Y. H. Teow and A. W. Mohammad, New generation nanomaterials for water desalination: a review, *Desalination*, 2019, **451**, 2–17.

24 T. D. Nguyen, *et al.*, Corrosion protection of carbon steel using hydrotalcite/graphene oxide nanohybrid, *J. Coat. Technol. Res.*, 2019, **16**, 585–595.

25 D. Nguyen, *et al.*, Influence of Graphene Oxide on the Corrosion Inhibition Effect of Hydrotalcite Loaded with 2-Benzothiazolythio-Succinic Acid, *Vietnam J. Sci. Technol.*, 2018, **56**, 19.

26 H. B. Mohd Sidek, Y. K. Jo, I. Y. Kim and S.-J. Hwang, Stabilization of Layered Double Oxide in Hybrid Matrix of Graphene and Layered Metal Oxide Nanosheets: An Effective Way to Explore Efficient CO_2 Adsorbent, *J. Phys. Chem. C*, 2016, **120**, 23421–23429.

27 D. Iruretagoyena, M. S. P. Shaffer and D. Chadwick, Layered Double Oxides Supported on Graphene Oxide for CO_2 Adsorption: Effect of Support and Residual Sodium, *Ind. Eng. Chem. Res.*, 2015, **54**, 6781–6792.

28 A. Garcia-Gallastegui, *et al.*, Graphene Oxide as Support for Layered Double Hydroxides: Enhancing the CO_2 Adsorption Capacity, *Chem. Mater.*, 2012, **24**, 4531–4539.

29 X.-L. Wu, L. Wang, C.-L. Chen, A.-W. Xu and X.-K. Wang, Water-dispersible magnetite-graphene-LDH composites for efficient arsenate removal, *J. Mater. Chem.*, 2011, **21**, 17353–17359.

30 X. Yuan, *et al.*, Calcined graphene/MgAl-layered double hydroxides for enhanced Cr(VI) removal, *Chem. Eng. J.*, 2013, **221**, 204–213.

31 M. K. Kumar, K. C. Swaathini, N. S. Jha and S. K. Jha, Facile In Situ Electrosynthesis and High Electrocatalytic Performance of Interconnected Layered Double Hydroxides/Graphene Hybrids for Dopamine Oxidation: A Comparative Study, *Electroanalysis*, 2019, **31**, 485–495.

32 M. G. Álvarez, D. Tichit, F. Medina and J. Llorca, Role of the synthesis route on the properties of hybrid LDH-graphene as basic catalysts, *Appl. Surf. Sci.*, 2017, **396**, 821–831.

33 N. S. Ahmed, *et al.*, Graphene-oxide-supported CuAl and CoAl layered double hydroxides as enhanced catalysts for carbon-carbon coupling via Ullmann reaction, *J. Solid State Chem.*, 2017, **246**, 130–137.

34 Y.-F. Yu, V. Parthiban and K.-Y. Huang, Effective Corrosion Protection Coatings of Polyaniline/Gamma-Alumina Nanocomposites, *Sens. Mater.*, 2017, **29**, 1531–1544.

35 L. Huang, *et al.*, Facile preparation of flower-like NiMn layered double hydroxide/reduced graphene oxide microsphere composite for high-performance asymmetric supercapacitors, *J. Alloys Compd.*, 2018, **730**, 71–80.

36 G. B. B. Varadwaj and V. O. Nyamori, Layered double hydroxide- and graphene-based hierarchical nanocomposites: synthetic strategies and promising applications in energy conversion and conservation, *Nano Res.*, 2016, **9**, 3598–3621.

37 C. Chen, *et al.*, Synergistic effect of graphene oxide@phosphate-intercalated hydrotalcite for improved anti-corrosion and self-healable protection of waterborne epoxy coating in salt environments, *J. Mater. Chem. C*, 2019, **7**, 2318–2326.

38 W. Yang, Y. Xia, X. Liu, J. Yang and Y. Liu, Layered double hydroxides/reduced graphene oxide nanocomposites with enhanced barrier properties, *Polym. Compos.*, 2018, **39**, 3841–3848.

39 W. Sun, T. Wu, L. Wang, C. Dong and G. Liu, Controlled Preparation of MgAl-Layered Double Hydroxide/Graphene Hybrids and their Applications for Metal Protection, *Ind. Eng. Chem. Res.*, 2019, **58**, 16516–16525.

40 D. W. Deberry, Modification of the Electrochemical and Corrosion Behavior of Stainless Steels with an, *Electroactive Coating*, 1985, 1022–1026.

41 B. Wessling, Corrosion Prevention with an Organic Metal (Polyaniline): Surface Ennobling, Passivation, Corrosion Test Results, *Mater. Corros.*, 1996, **47**(8), 439–445.

42 B. Z. Jugovi, A. R. Elkais and M. M. Gvozdenovi, The influence of thin benzoate-doped polyaniline coatings on corrosion protection of mild steel in different environments, *Prog. Org. Coat.*, 2013, **76**, 670–676.

43 M. Kendig, M. Hon and L. Warren, 'Smart' corrosion inhibiting coatings, *Prog. Org. Coat.*, 2003, **47**, 183–189.

44 S. D. Souza, *Smart coating based on polyaniline acrylic blend for corrosion protection of different metals*, 2007, vol. 201, pp. 7574–7581.

45 R. M. Torresi, S. D. Souza, E. Pereira, I. C. Susana and D. Torresi, Galvanic coupling between metal substrate and polyaniline acrylic blends: corrosion protection mechanism, *Electrochim. Acta*, 2005, **50**, 2213–2218.

46 M. Hon and M. Kendig, Environmentally Triggered Release of Oxygen-Reduction Inhibitors from Inherently Conducting Polymers, *Corrosion*, 2004, **60**(11), 1024.

47 P. J. Kinlen, Y. Ding and D. C. Silverman, *Corrosion Protection of Mild Steel Using Sulfonic and Phosphonic Acid-Doped Polyanilines*, 2002, pp. 490–497.

48 E. P. Silva, S. I. Co, M. L. A. Temperini and R. M. Torresi, *Polyaniline Based Acrylic Blends for Iron Corrosion Protection Polyaniline Based Acrylic Blends for Iron Corrosion Protection*, 2001, DOI: DOI: 10.1149/1.1381288.

49 J. E. Pereira da Silva, S. I. Córdoba de Torresi and R. M. Torresi, Polyaniline acrylic coatings for corrosion inhibition: the role played by counter-ions, *Corros. Sci.*, 2005, **47**, 811–822.

50 M. Gvozdenović, E. Džunuzović, B. Jugović and B. Grgur, Polyaniline based corrosion inhibitors for conventional organic coatings, *Zast. Mater.*, 2018, **59**(2), 282–292.

51 J. A. Syed, S. Tang, H. Lu and X. Meng, Water-Soluble Polyaniline–Polyacrylic Acid Composites as Efficient Corrosion Inhibitors for 316SS, *Ind. Eng. Chem. Res.*, 2015, **54**, 2950–2959.

52 Y. Yi, G. Liu, Z. Jin and D. Feng, The Use of Conducting Polyaniline as Corrosion Inhibitor for Mild Steel in Hydrochloric Acid, *Int. J. Electrochem. Sci.*, 2013, **8**, 3540–3550.

53 N. Pirhady Tavandashti, *et al.*, pH-Responsive Nanostructured Polyaniline Capsules for Self-Healing Corrosion Protection: The Influence of Capsule Concentration, *Sci. Iran.*, 2017, **24**, 3512–3520.

54 R. Ansari and A. H. Alikhani, Application of polyaniline/nylon composites coating for corrosion protection of steel, *J. Coat. Technol. Res.*, 2009, **6**, 221–227.

55 M. Rashid, S. Sabir, A. A. Rahim and U. Waware, Polyaniline/Palm Oil Blend for Anticorrosion of Mild Steel in Saline Environment, *J. Appl. Chem.*, 2014, **2014**, 973653.

56 K. Jlassi, *et al.*, Anti-corrosive and oil sensitive coatings based on epoxy/polyaniline/magnetite-clay composites through diazonium interfacial chemistry, *Sci. Rep.*, 2018, **8**, 13369.

57 P. Guoxiang, *et al.*, Preparation of CoAl layered double hydroxide nanoflake arrays and their high supercapacitance performance, *Appl. Clay Sci.*, 2014, **102**, 28–32.

58 X.-R. Zeng and T.-M. Ko, Structure–conductivity relationships of iodine-doped polyaniline, *J. Polym. Sci., Part B: Polym. Phys.*, 1997, **35**, 1993–2001.

59 P. K. Khanna, *et al.*, Synthesis of HCl doped polyaniline–CdS nanocomposite by use of organometallic cadmium precursor, *Mater. Chem. Phys.*, 2006, **95**, 24–28.

60 C. Muthuselvi, S. Buvaneswari and N. Bashariya, Single Diffusion Gel Growth, Spectral and Antimicrobial Activity Studies on 4-Carboxyaniline Crystal, *Asian J. Appl. Sci. Technol.*, 2017, **1**, 194–206.

61 M. M. Daouadji and N. Chelali, Influence of molecular weight of poly(ortho-ethoxyaniline) on the corrosion inhibition efficiency of mild steel in acidic media, *J. Appl. Polym. Sci.*, 2004, **91**, 1275–1284.

62 D. W. DeBerry, Modification of the Electrochemical and Corrosion Behavior of Stainless Steels with an Electroactive Coating, *J. Electrochem. Soc.*, 1985, **132**, 1022–1026.

63 B. Wessling, Corrosion prevention with an organic metal (polyaniline): surface ennobling, passivation, corrosion test results, *Mater. Corros.*, 1996, **47**, 439–445.

64 L. Cecchetto, *et al.*, Emeraldine base as corrosion protective layer on aluminium alloy AA5182, effect of the surface microstructure, *Corros. Sci.*, 2007, **49**, 818–829.

65 P. P. Deshpande and D. Sazou, Corrosion Protection of Metals by Intrinsically Conducting Polymers, *CRC Press*, 2016, **214**(41), 919–920.

66 A. Dominis, G. Spinks and G. Wallace, Comparison of polyaniline primers prepared with different dopants for corrosion protection of steel, *Prog. Org. Coat.*, 2003, **48**, 43–49.

67 J. Fang, K. Xu, L. Zhu, Z. Zhou and H. Tang, A study on mechanism of corrosion protection of polyaniline coating and its failure, *Corros. Sci.*, 2007, **49**, 4232–4242.

68 Y. Li, H. Zhang, X. Wang, J. Li and F. Wang, Role of dissolved oxygen diffusion in coating defect protection by emeraldine base, *Synth. Met.*, 2011, **161**, 2312–2317.

69 A. R. Elkais, M. M. Gvozdenović, B. Z. Jugović and B. N. Grgur, The influence of thin benzoate-doped polyaniline coatings on corrosion protection of mild steel in different environments, *Prog. Org. Coat.*, 2013, **76**, 670–676.

70 T. D. Nguyen, *et al.*, Mechanism for protection of iron corrosion by an intrinsically electronic conducting polymer, *J. Electroanal. Chem.*, 2004, **572**, 225–234.

71 M. Kendig and M. Hon, Environmentally Triggered Release of Oxygen-Reduction Inhibitors from Inherently Conducting Polymers, *Corrosion*, 2004, **60**, 1024–1033.

72 D. Sazou and P. P. Deshpande, Conducting polyaniline nanocomposite-based paints for corrosion protection of steel, *Chemical Papers*, 2017, **71**, 459–487.

73 J. Dong, W. Pan, J. Luo and R. Liu, Synthesis of inhibitor-loaded polyaniline microcapsules with dual anti-corrosion functions for protection of carbon steel, *Electrochim. Acta*, 2020, **364**, 137299.

74 H. Wu, L. Zhang, Y. Zhang, S. Long and X. Jie, Corrosion behavior of Mg–Al LDH film in situ assembled with graphene on Mg alloy pre-sprayed Al layer, *J. Alloys Compd.*, 2020, **834**, 155107.

75 N. T. Duong, T. B. An, P. T. Thao, V. K. Oanh and T. A. Truc, Corrosion protection of carbon steel by polyurethane coatings containing graphene oxide, *Vietnam J. Chem.*, 2020, **58**, 108–112.